

Radar Soundings of the Ionosphere of Mars

D. A. Gurnett,^{1*} D. L. Kirchner,¹ R. L. Huff,¹ D. D. Morgan,¹
A. M. Persoon,¹ T. F. Averkamp,¹ F. Duru,¹ E. Nielsen,²
A. Safaeinili,³ J. J. Plaut,³ G. Picardi⁴

We report the first radar soundings of the ionosphere of Mars with the MARSIS (Mars Advanced Radar for Subsurface and Ionosphere Sounding) instrument on board the orbiting Mars Express spacecraft. Several types of ionospheric echoes are observed, ranging from vertical echoes caused by specular reflection from the horizontally stratified ionosphere to a wide variety of oblique and diffuse echoes. The oblique echoes are believed to arise mainly from ionospheric structures associated with the complex crustal magnetic fields of Mars. Echoes at the electron plasma frequency and the cyclotron period also provide measurements of the local electron density and magnetic field strength.

The Mars Express spacecraft (*1*), currently in orbit around Mars, carries a low-frequency radar (*2*) called MARSIS. Here, we present the first ionospheric sounding results from MARSIS. Spacecraft radar sounders were originally developed in the 1960s to study Earth's ionosphere (*3–5*) and have proven to be a powerful tool for studying ionospheric physics. Currently, most of our knowledge of the Martian ionosphere comes from radio occultation measurements, which provide an average electron density along a line of sight from Earth to a spacecraft in orbit around Mars (*6–9*). The MARSIS measurements nicely complement these measurements by providing better spatial resolution and the ability to make observations in regions where radio occultation measurements cannot be made. Because of geometric constraints imposed by the orbits of Earth and Mars, radio occultation measurements are restricted to solar zenith angles from about 48° to 132°.

A horizontally stratified ionosphere provides an almost perfectly reflecting surface for radio echo sounding. The reflection (Fig. 1) occurs because free-space electromagnetic radiation cannot propagate at frequencies below the electron plasma frequency (*10*), which is given by $f_p = 8980\sqrt{n_e}$ Hz, where n_e is the electron number density in cm^{-3} . The MARSIS ionospheric soundings are carried out by transmitting a short pulse at a frequency f and then measuring the time delay, Δt , for the echo to return. The time delay is measured as a function of frequency by sequentially stepping the transmission frequency over the frequency

range of interest. Three types of echoes usually occur (Fig. 1). The first is a very strong “spike” at the local electron plasma frequency, $f_p(\text{local})$. This response is caused by excitation of electrostatic oscillations at the electron plasma frequency (*10*). The second is an echo from the ionosphere that extends from $f_p(\text{local})$ to the maximum plasma frequency in the ionosphere, $f_p(\text{max})$, above which the radio wave can penetrate through the ionosphere to the surface. The third is a surface reflection that extends from $f_p(\text{max})$ to the maximum sounding frequency. The ionospheric echo and the surface reflection come together in a sharply defined cusp, centered on $f_p(\text{max})$. The cusp occurs because the propagation speed of the wave packet (i.e., the group velocity) is very small over an increasingly long path length as the wave frequency approaches $f_p(\text{max})$.

Observations. The Mars Express spacecraft is in an eccentric orbit around Mars with a periapsis altitude of about 275 km, an apoapsis altitude of about 10,100 km, an orbital inclination of 86°, and a period of 6.75 hours. A typical MARSIS ionospheric sounding pass lasts about 40 min and starts at an altitude of about 1200 km on the inbound leg, extends through periapsis, and ends at an altitude of about 1200 km on the outbound leg. Because of gravitational perturbations, the local time and latitude of periapsis evolve rather rapidly. Most of the data collected so far (June to October 2005) have been from the day side of Mars, although a small amount is available from the night side near the evening terminator. The ionospheric soundings are typically displayed in the form of an ionogram, which is a plot of the echo strength versus frequency and time delay. Two ionograms (Fig. 2) have been selected to illustrate the range of phenomena typically observed. The closely spaced vertical lines in the upper left corner of the first ionogram (Fig. 2A) are at harmonics of the local electron plasma frequency and are caused by the excitation of electron plasma oscillations, in this case at a frequency that is slightly below the low-frequency cutoff (100 kHz) of the receiver. Even though the fundamental of the plasma frequency is not observed directly in this case, the plasma frequency can still be determined from the spacing of the harmonics and is $f_p(\text{local}) = 44$ kHz. At somewhat higher frequencies, from about 0.5 to 1.7 MHz, a strong, well-defined ionospheric echo can be seen with time delays ranging from about 4 to 5 ms. At even higher frequencies, from about 1.7 to 5.5 MHz, a strong reflected signal from the surface of Mars is apparent. The maximum plasma frequency in the ionosphere, $f_p(\text{max})$, can be identified from the cusp and is 1.71

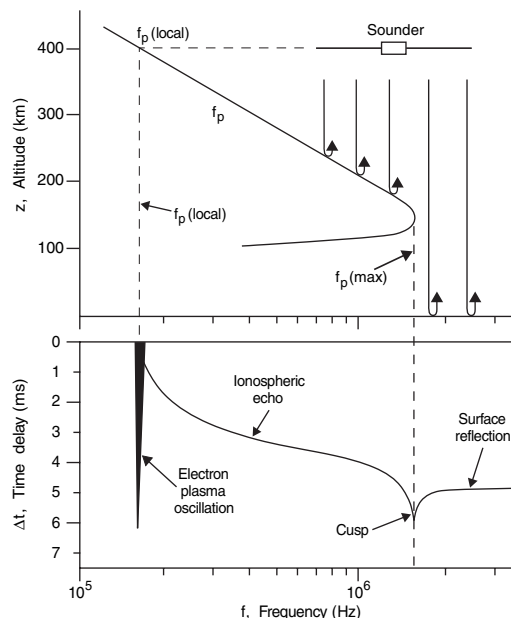


Fig. 1. The top panel shows a representative profile of the electron plasma frequency f_p in the martian ionosphere as a function of altitude z , and the bottom panel shows the corresponding ionogram, which is a plot of the delay time Δt for a sounder pulse at a frequency f to reflect and return to the spacecraft. The intense vertical “spike” at the local electron plasma frequency, $f_p(\text{local})$, is caused by electron plasma oscillations excited by the sounder pulse. At frequencies from $f_p(\text{local})$ to the maximum frequency in the ionosphere, $f_p(\text{max})$, an ionospheric echo is detected, followed at higher frequencies by a reflection from the surface. The ionospheric echo trace and the surface reflection trace form a cusp centered on $f_p(\text{max})$.

¹Department of Physics and Astronomy, University of Iowa, Iowa City, IA 52242, USA. ²Max Planck Institute for Solar System Research, 37191 Katlenburg-Lindau, Germany. ³Jet Propulsion Laboratory, Pasadena, CA 91109, USA. ⁴Infocom Department, “La Sapienza” University of Rome, 00184 Rome, Italy.

*To whom correspondence should be addressed.
E-mail: donald-gurnett@uiowa.edu

MHz. An unexpected feature is the presence of a second ionospheric echo with time delays ranging from about 6.3 to 7.1 ms. This echo has to arise from an oblique reflection, because the apparent range ($c\Delta t/2$, where c is the speed of light) given on the right side of the spectrogram is substantially greater than the distance to either the ionosphere or the surface. The origin of such oblique echoes will be discussed later.

Another unexpected effect, consisting of a series of echoes equally spaced in time, is seen along the left edge of the second ionogram (Fig. 2B). Comparisons of these echoes with the magnetic field model of Cain *et al.* (11) show that the repetition rate of these echoes, $1/T_c$, is almost exactly the local electron cyclotron frequency, $f_c = 28 B$ Hz, where B is the magnetic field strength in nT. Because of the close relation to the electron cyclotron frequency, these echoes are called “electron cyclotron echoes.” Such echoes are very common and are usually present whenever the magnetic field strength is greater than a few tens of nT. We believe that these echoes are caused by electrons accelerated by the strong electric fields near the antenna during each cycle of the transmitter waveform. The cyclotron motion of the electrons in the local magnetic field then causes these electrons to periodically return to the vicinity of the antenna, where they induce a signal on the antenna. For this process to occur, the magnetic field strength must be reasonably uniform over a spatial region comparable to the cyclotron radius. For a magnetic field strength of 100 nT, which is a typical crustal field strength at the spacecraft, and a voltage of 500 V, which is the typical antenna voltage, the cyclotron radius is about 1 km. Because the crustal magnetic fields have scale sizes of hundreds of kilometers, this condition is easily satisfied.

In contrast to the first ionogram (Fig. 2A), no surface reflection can be detected in the second ionogram (Fig. 2B). The intensity of the surface reflection is found to be highly variable, a topic of considerable importance for subsurface sounding. Some of this variability can be attributed to solar activity. For example, surface reflections disappeared completely about 2 days after a class X17 solar flare that occurred on 7 September 2005 and did not reappear until 23 September, nearly 2 weeks later. Although further analysis is needed, it seems almost certain that the absorption is caused by energetic charged particles produced by solar flares. The onset of the absorption is usually delayed by a day or more after a flare and tends to last many days, much longer than the typical time scale for decay of the ultraviolet and x-ray radiation associated with a flare. At Earth it is well known that energetic protons from solar flares cause enhanced ionization and absorption of radio waves in the lower levels of the ionosphere

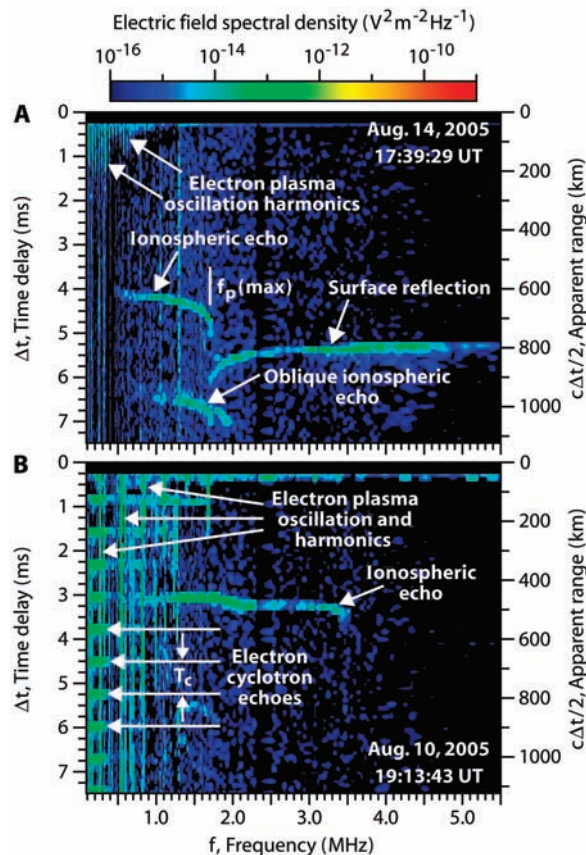


Fig. 2. Two ionograms selected to illustrate typical features found in the MARSIS ionospheric soundings. The ionograms display echo strength (color coded) as a function of frequency f and time delay Δt , with time delay plotted positive downward along the vertical axis. The apparent range to the reflection point $c\Delta t/2$, where c is the speed of light, is shown on the right. Ionogram (A) was obtained near the evening terminator at a solar zenith angle of $\chi = 89.3^\circ$ and an altitude of 778 km. Ionogram (B) was obtained on the day side at a solar zenith angle of $\chi = 47.9^\circ$ and an altitude of 573 km. Electron plasma oscillation harmonics can be seen in both ionograms, as well as strong echoes from the ionosphere. Ionogram (B) has a series of horizontal, equally spaced echoes along the left side. These echoes occur at the electron cyclotron period and are called electron cyclotron echoes. They are believed to be caused by the cyclotron motion of electrons accelerated by the transmitter pulse. Although a strong surface reflection is present in (A), no surface reflection is present in (B). Surface reflections are seldom seen at solar zenith

angles less than about 40° or during periods of intense solar activity.

(12), and a similar process may occur at Mars. In addition to the solar flare control, the absorption also appears to increase with decreasing solar zenith angle. Even during periods of low solar activity, surface reflections are rarely observed when the solar zenith angle is less than about 40° .

Ionospheric density models. To compare the MARSIS ionospheric soundings to various ionospheric models, it is necessary to convert the soundings to usable electron density profiles. Although a rough estimate of the density profile can be obtained from the apparent range to the reflection point, for accurate measurements it is necessary to correct for dispersion, which is the effect the plasma has on the propagation speed of the wave. For vertical incidence on a horizontally stratified ionosphere, the round-trip delay time as a function of frequency, $\Delta t(f)$, is given by the integral

$$\Delta t(f) = \frac{2}{c} \int_{z(f_p)}^{z_{sc}} \frac{dz}{\sqrt{1 - \frac{f_p^2(z)}{f^2}}} \quad (1)$$

where the integration is carried out from the reflection point altitude, $z(f_p)$, to the spacecraft altitude, z_{sc} . Because $\Delta t(f)$ is known from the ionospheric echo trace, the basic problem is to invert the integral to obtain $z(f_p)$, i.e., the altitude of the reflection point as a function of the plasma frequency. Once this is known, the equation $f_p = 8980\sqrt{n_e}$ can be used to obtain

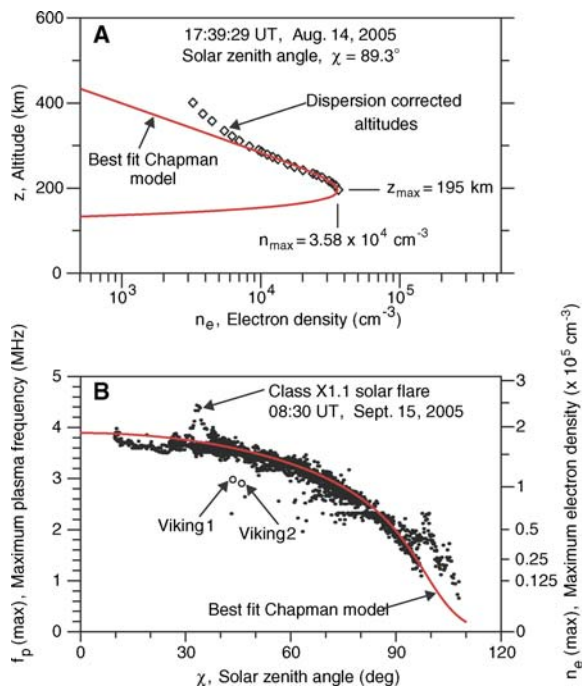
$z(n_e)$. Although the mathematical techniques for carrying out this inversion are straightforward, there are sometimes practical difficulties. For example, the ionospheric echo trace often does not extend down to the local plasma frequency (Fig. 2). In such cases it is necessary to make a reasonable guess as to how the echo trace extends from the lowest frequency measured to the local plasma frequency. Normally the inversion is not very sensitive to this choice, because the correction to the propagation speed becomes quite small when the plasma frequency is well below the wave frequency.

An example of an electron density profile obtained by inverting Eq. 1 is shown (Fig. 3A). This profile was obtained by using both the ionospheric echo trace and the surface reflection trace (Fig. 2A). Our approach was to select a theoretical model for the density profile and then adjust the parameters in the model to give the overall best fit to the measured time delays. For a density model, we use the following equation from Chapman (13)

$$n_e = n_0 \exp \left[\frac{1}{2} \left\{ 1 - \frac{z - z_0}{H} - \text{Ch}(x, \chi) \exp \left(-\frac{z - z_0}{H} \right) \right\} \right] \quad (2)$$

where z is the altitude, n_0 is the maximum electron density at the subsolar point, and z_0 is the altitude of this maximum. The function

Fig. 3. Two illustrations comparing electron densities obtained from ionospheric soundings to the Chapman (73) ionospheric density model. The diamond-shaped points in (A) give the electron density profile computed from the ionospheric echo trace in Fig. 2A after correcting for dispersion. The red curve gives the best fit to this density profile, while simultaneously providing a good fit to the surface reflection trace. The best-fit parameters are $n_0 = 1.32 \times 10^5 \text{ cm}^{-3}$, $z_0 = 130 \text{ km}$, $z_{\text{max}} = 195 \text{ km}$, $n_{\text{max}} = 3.58 \times 10^4 \text{ cm}^{-3}$, $H = 25 \text{ km}$, $x = 141$, and $\text{Ch}(x, \chi) = 13.5$. Plot (B) shows the maximum plasma frequency in the ionosphere, $f_p(\text{max})$, as a function of solar zenith angle χ for 12 randomly selected orbits. The corresponding electron density is shown on the right side of the plot. The red line is the best fit to the Chapman electron density model using $(q_0/\alpha)^{1/2} = 1.98 \times 10^5 \text{ cm}^{-3}$.



$\text{Ch}(x, \chi)$ is called Chapman's grazing incidence function and takes into account the absorption of the solar radiation as it passes obliquely through the atmosphere. This function depends on the solar zenith angle χ and a dimensionless parameter $x = (R_M + z_0)/H$, where $R_M = 3396 \text{ km}$ is the radius of Mars, and H is the scale height of the neutral atmosphere. $\text{Ch}(x, \chi)$ can be computed from a power series (13) or from a table provided by Wilkes (14). The fit to the top-side electron density profile is very good (Fig. 3A). The maximum electron density, $n_{\text{max}} = 3.58 \times 10^4 \text{ cm}^{-3}$, and the altitude of the maximum, $z_{\text{max}} = 195 \text{ km}$, are in reasonable agreement with radio occultation results at this solar zenith angle (6, 7). Although the bottom-side electron density profile cannot be expected to represent complicated features such as multiple density layers, the model does accurately represent the top-side electron density profile near the peak and the total electron content (TEC) through the ionosphere, which is determined by the dispersion of the surface reflection. The total electron content is defined as the integral $\int n_e dz$ along a vertical line through the ionosphere and, in this case, is $\text{TEC} = 3.7 \times 10^{11} \text{ cm}^{-2}$. The deviation of the measured electron densities from the model at altitudes above about 300 km is probably caused by upward diffusion of plasma away from the region of photochemical equilibrium described by Chapman's model.

To study the dependence of the maximum electron density n_{max} on the solar zenith angle χ , the maximum frequencies of the ionospheric echo traces have been measured for 12 randomly selected passes from 5 July to 10 October 2005. During this time, the solar zenith angle at periaapsis systematically decreased

from 98° to 16° , thereby providing a good sampling of solar zenith angles. A scatter plot of the measured $f_p(\text{max})$ values is shown (Fig. 3B) as a function of solar zenith angle. As can be seen, the maximum plasma frequency has a very clear systematic dependence on solar zenith angle, varying from about 3.9 MHz near the subsolar point to less than 1 MHz on the night side. A scale showing the corresponding electron density values is given on the right side of the plot. These electron densities are in good agreement with the results from radio occultation measurements (6, 7) but slightly higher than the in situ Viking 1 and 2 measurements (15), which were obtained during a less active phase of the solar cycle.

The solar zenith angle dependence (Fig. 3B) can be compared directly with the predictions of Chapman's electron density model. In Chapman's model, the maximum electron density in the ionosphere is given by

$$n_e(\text{max}) = (q_0/\alpha)^{1/2}/\text{Ch}(x, \chi)^{1/2} \quad (3)$$

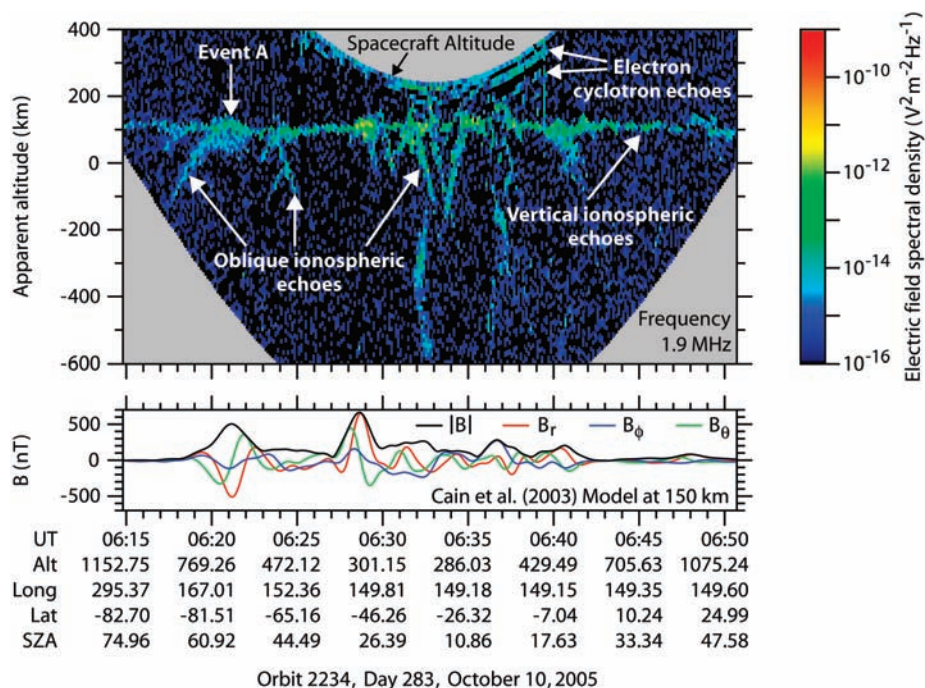
where q_0 is the ionization rate at the subsolar point and α is the recombination rate. The best fit of this equation to the measured $n_e(\text{max})$ values is shown by the red line. This fit uses the same basic parameters as in the first fit (Fig. 3A), with the exception of the parameter $(q_0/\alpha)^{1/2} = 1.98 \times 10^5 \text{ cm}^{-3}$, which has been adjusted to give the best overall fit. The fit has been purposely selected near the most dense cluster of points, ignoring the outlying points. The outlying points are almost certainly influenced by solar events. For example, the sharp peak in the density that occurred during a pass at a solar zenith angle of about 34° coincides with a class X1.1 solar flare that

occurred at 08:30 UT (Universal Time) on 15 September 2005. The enhanced electron densities during this event are almost certainly caused by an intense burst of ultraviolet radiation arriving from the Sun. Other large enhancements, well above the electron densities predicted by Chapman's equation, can also be seen on the night side at solar zenith angles of 98° and 104° . These events are not associated with any known solar flare activity. The ionospheric echoes in this region are often very diffuse and sometimes have unusual characteristics, such as a surface reflection that extends below the ionospheric echo trace. Such echoes are impossible in a horizontally stratified ionosphere and are suggestive of considerable small-scale structure, possibly consisting of low density "holes" like those that have been observed on the night side of Venus (16).

Oblique echoes. Oblique ionospheric echoes (Fig. 2A) are a common feature in the MARSIS ionograms. Inspection of successive ionograms shows that the range of these echoes systematically either increases or decreases with increasing time and sometimes merges with the vertical echoes. A good way to study these echoes is to make a plot of the echo strength at a fixed frequency as a function of time and apparent altitude (Fig. 4). Apparent altitude is defined as the spacecraft altitude minus the apparent range. In this display, the vertical echo is the nearly horizontal line at an altitude of about 120 km. The oblique echoes almost always have the shape of a downward-facing hyperbola, sometimes consisting of both branches, but more frequently consisting of only one branch or part of a branch. Sometimes the apex of the hyperbola merges with the vertical echo, as in the event marked A. In a radar display of this type, hyperbola-shaped echoes are characteristic of relative motion between the radar and an off-vertical target. The asymptotic slopes of the hyperbola-shaped echoes are consistent with the motion of the spacecraft relative to a feature that is fixed with respect to Mars. We have verified this hypothesis by comparing repeated passes over the same region of Mars. Such comparisons show that nearly identical hyperbola-shaped features often reappear over the same region. The ones that do not show a good pass-to-pass correlation often occur in very complicated regions with many overlapping echoes, such as near the center of Fig. 4.

Strong evidence exists that most of the oblique ionospheric echoes are related to ionospheric density structures caused by the crustal magnetic fields discovered by the Mars Global Surveyor spacecraft (17–19). In a comparison (bottom panel of Fig. 4) with the crustal magnetic field computed at an altitude of 150 km using the global magnetic field model developed by Cain *et al.* (11), the oblique echoes are seen to occur in the region where strong magnetic fields are present. Inspection of other

Fig. 4. The top panel shows echo strengths at a frequency of 1.9 MHz plotted as a function of time and apparent altitude, which is the spacecraft altitude minus the apparent range of the echo. The bottom panel shows three components, B_r , B_θ , and B_ϕ , of the crustal magnetic field and the magnitude of the magnetic field, $|B|$, computed from the Cain *et al.* magnetic field model at an altitude of 150 km. The nearly horizontal echoes at an altitude of about 120 km are vertical echoes, and the downward-facing hyperbola-shaped features are oblique echoes. This and other similar examples provide strong evidence that density structures related to crustal magnetic fields are responsible for most of the oblique echoes.



similar plots confirms this basic relationship. Although the detailed correlation between the oblique echoes and the magnetic field is often complicated and difficult to resolve, in some cases, such as event A in Fig. 4, the relationship is quite clear. For this event, the apex of the hyperbola-shaped echo is coincident with a well-defined peak in the magnetic field. Furthermore, near the apex, the altitude of the oblique echo (which has merged with the vertical echo) is clearly seen to be greater than the altitude of the surrounding ionosphere, which indicates an upward bulge in the ionosphere. Note also that the magnetic field is nearly vertical in this region, as can be seen by the radial (vertical) component, B_r , which is much stronger than either the southward, B_θ , or eastward, B_ϕ , components. These and numerous other similar observations lead us to conclude that the oblique echoes usually arise from an upward bulge in the ionosphere in a region where the magnetic field is nearly vertical (Fig. 5A). As the spacecraft approaches the bulge, oblique echoes start as soon as the constant density surface ($f = f_p$) is normal to the line of sight from the spacecraft (Fig. 5B). Two echoes are then detected until the spacecraft is nearly over the bulge, at which point the vertical echo disappears or merges with the oblique echo as the spacecraft passes over the bulge. This basic model is consistent with radar occultation measurements that show an increase in the scale height in regions where the crustal magnetic field is nearly vertical (20–23). The bulge is believed to be due to heating and the resulting increase in the scale height, caused by solar wind electrons that have access to the lower levels of the ion-

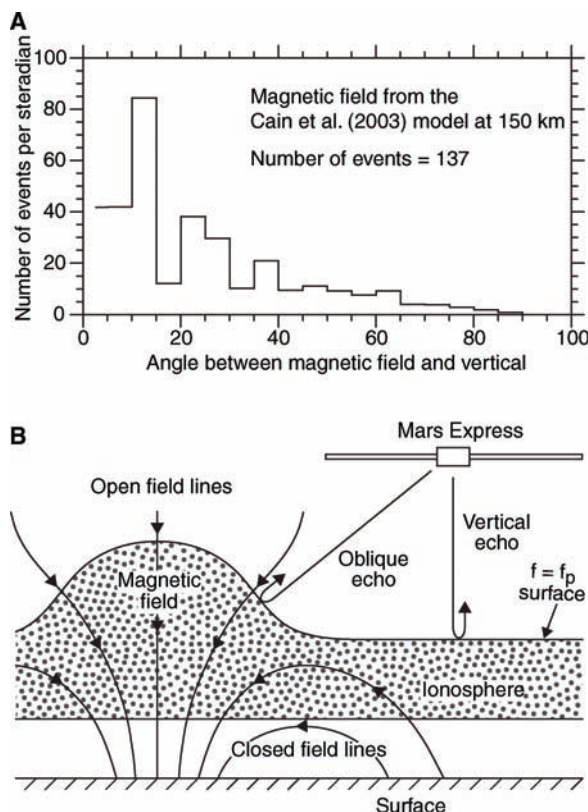


Fig. 5. (A) The distribution of oblique echo events as a function of the angle between the magnetic field and vertical. The angles were evaluated at the apex of the hyperbola-shaped time delay feature using the Cain *et al.* model. Most of the events occur at angles less than about 40°, indicating that the density structures responsible for the oblique echoes tend to occur in regions where the magnetic field is nearly vertical. (B) A sketch of the ionospheric density structures that are thought to be responsible for the oblique ionospheric echoes. As the spacecraft approaches the bulge in the ionosphere, the sounder detects two echoes, a vertical echo from the ionosphere and an oblique echo from the bulge. As the spacecraft passes over the bulge, the vertical echo either merges with the oblique echo or disappears entirely, depending on the exact shape of the bulge. The bulge in the ionosphere is believed to be due to ionospheric heating caused by hot solar wind electrons that reach the lower levels of the ionosphere along open magnetic field lines.

osphere along open magnetic field lines (20, 23). More complex structures probably exist in regions where the magnetic field is very complex, such as near the middle of the plot in Fig. 4, or in regions where the crustal magnetic fields are strong enough to stand off the solar wind (24).

Although crustal magnetic fields are almost certainly involved in producing the majority of the oblique echoes, cases have been found where the echoes exist in regions where the Cain *et al.* model does not predict detectable crustal magnetic fields. We do not know if these cases involve a failure of the Cain *et al.*

model or whether there are other mechanisms for producing such echoes. Possible mechanisms are wind-driven atmospheric waves excited by topographic features and various types of wavelike structures in the ionosphere driven by interactions with the solar wind.

Conclusion. The MARSIS ionospheric soundings have shown that the ionosphere of Mars is in good agreement with the expectations of Chapman's 1931 photoequilibrium theory for the origin of planetary ionospheres. The soundings have also revealed a number of unexpected features. These include echoes that reoccur at the electron cyclotron period, large variations in the absorption apparently caused by energetic solar events, oblique echoes caused by ionospheric structures associated with the crustal magnetic fields of Mars, diffuse echoes apparently caused by scattering from ionospheric irregularities, and ionospheric holes. Because the subsurface soundings must occur at frequencies well above the maximum electron plasma frequency in the ionosphere and under conditions of low ionospheric absorption, these measurements have already proved to be quite useful for planning subsurface sounding op-

erations. The electron cyclotron echoes also provide a new method of measuring the local magnetic field strength, which is useful because Mars Express does not have a magnetometer.

References and Notes

1. A. Chicaro, P. Martin, R. Traunter, *Mars Express: A European Mission to the Red Planet, SP-1240* (European Space Agency Publication Division, Noordwijk, Netherlands, 2004).
2. G. Picardi *et al.*, *Mars Express: A European Mission to the Red Planet, SP-1240* (European Space Agency Publication Division, Noordwijk, Netherlands, 2004).
3. C. A. Franklin, M. A. Maclean, *Proc. IEEE* **57**, 897 (1969).
4. E. L. Hagg, E. J. Hewens, G. L. Nelms, *Proc. IEEE* **57**, 949 (1969).
5. W. Calvert, J. R. McAfee, *Proc. IEEE* **57**, 1019 (1969).
6. M. H. G. Zhang, J. G. Luhmann, A. J. Kliore, *J. Geophys. Res.* **95**, 17095 (1990).
7. J. G. Luhmann, L. H. Brace, *Rev. Geophys.* **29**, 121 (1991).
8. D. P. Hinson, G. L. Tyler, L. J. Hollingsworth, R. J. Wilson, *J. Geophys. Res.* **106**, 1463 (2001).
9. M. Pätzold *et al.*, *Science* **310**, 837 (2005).
10. D. A. Gurnett, A. Bhattacharjee, *Introduction to Plasma Physics* (Cambridge Univ. Press, Cambridge, 2005), p. 114.
11. J. C. Cain, B. B. Ferguson, D. Mozzoni, *J. Geophys. Res.* **108** (E2), 5008 10.1029/2000JE001487 (2003).
12. J. D. Patterson, T. P. Armstrong, C. M. Laird, D. L. Detrick, A. T. Weatherwax, *J. Geophys. Res.* **106**, 149 (2001).
13. S. Chapman, *Proc. Phys. Soc.* **43**, 483 (1931).
14. M. V. Wilkes, *Proc. R. Soc. London B. Biol. Sci.* **67**, 304 (1954).
15. W. B. Hanson, S. Sanatani, D. R. Zuccaro, *J. Geophys. Res.* **82**, 4351 (1977).
16. L. H. Brace *et al.*, in *Venus*, D. M. Hunten, L. Colin, T. M. Donahue, V. I. Moroz, Eds. (Univ. of Arizona Press, Tucson, AZ, 1983), pp. 779–840.
17. M. H. Acuña *et al.*, *Science* **279**, 1676 (1998).
18. M. H. Acuña *et al.*, *Science* **284**, 790 (1999).
19. J. E. P. Connerney *et al.*, *Geophys. Res. Lett.* **28**, 4015 (2001).
20. N. F. Ness *et al.*, *J. Geophys. Res.* **105**, 15991 (2000).
21. A. M. Krymskii *et al.*, *J. Geophys. Res.* **107** (A9), 1245, 10.1029/2001JA000239 (2002).
22. A. M. Krymskii, T. K. Breus, N. F. Ness, D. P. Hinson, D. I. Bojkov, *J. Geophys. Res.* **108** (A12), 1431, 10.1029/2002JA009662 (2003).
23. A. M. Krymskii *et al.*, *J. Geophys. Res.* **109**, A11306, 10.1029/2004JA010420 (2004).
24. D. L. Mitchell *et al.*, *J. Geophys. Res.* **106**, 23419 (2001).
25. We thank the many members of scientific, technical, and management teams at NASA, the European Space Agency, the Italian Space Agency, and various industry groups for their considerable effort in making this project a success. The research at the University of Iowa was supported by NASA through contract 1224107 with the Jet Propulsion Laboratory.

26 October 2005; accepted 22 November 2005

Published online 30 November 2005;

10.1126/science.1121868

Include this information when citing this paper.

Animal Evolution and the Molecular Signature of Radiations Compressed in Time

Antonis Rokas,* Dirk Krüger,† Sean B. Carroll‡

The phylogenetic relationships among most metazoan phyla remain uncertain. We obtained large numbers of gene sequences from metazoans, including key understudied taxa. Despite the amount of data and breadth of taxa analyzed, relationships among most metazoan phyla remained unresolved. In contrast, the same genes robustly resolved phylogenetic relationships within a major clade of Fungi of approximately the same age as the Metazoa. The differences in resolution within the two kingdoms suggest that the early history of metazoans was a radiation compressed in time, a finding that is in agreement with paleontological inferences. Furthermore, simulation analyses as well as studies of other radiations in deep time indicate that, given adequate sequence data, the lack of resolution in phylogenetic trees is a signature of closely spaced series of cladogenetic events.

Detailed knowledge of the phylogenetic relationships among Metazoa and their eukaryotic relatives is critical for understanding the history of life and the evolution of molecules, phenotypes, and developmental mechanisms.

Howard Hughes Medical Institute, Laboratory of Molecular Biology, R. M. Bock Labs, University of Wisconsin–Madison, 1525 Linden Drive, Madison, WI 53706, USA.

*Present address: The Broad Institute of MIT and Harvard, 320 Charles Street, Cambridge, MA 02141, USA.

†Present address: Departments of Bacteriology and Plant Pathology, University of Wisconsin–Madison, 420 Henry Mall, Madison, WI 53706, USA.

‡To whom correspondence should be addressed. E-mail: sbcarrol@wisc.edu

Currently, with the exception of the well-resolved phylogenetic history of the deuterostomes (1), the relationships between and within protostome and diploblastic metazoan phyla remain unresolved (2–5). The uncertainty surrounding metazoan relationships may result from analytical and biological factors such as insufficient amounts of available sequence data, mutational saturation, the occurrence of unequal rates of evolution between lineages, or the rapidity with which metazoan phyla diversified (3–7).

Recent investigations concerning two critical variables of phylogenetic experimental design—the number of taxa and amount of data used—have guided our approach to meta-

zoan relationships. It has been shown that taxon number may not be as critical a determinant of phylogenetic accuracy (8, 9) as the choice of taxa (10). Thus, to investigate relationships among phyla at the base of the metazoan tree and within protostomes, we selected metazoans and closely related eukaryotes that included representatives from choanoflagellates, poriferans (one representative from each of the three poriferan classes), cnidarians (one representative from each of the three cnidarian classes), platyhelminths (two representatives), priapulids, annelids, mollusks, arthropods, nematodes, urochordates, and vertebrates (three representatives) (all taxa are listed in table S1).

The use of single or few genes is now recognized to be insufficient for the confident resolution of many clades (4, 11, 12). In contrast, analyses of larger amounts of data have robustly resolved relationships in many taxonomic groups (11–14), even after allowance for a high percentage of missing data (12–14). Thus, to increase resolution of metazoan relationships, we used experimental and bioinformatic approaches to assemble a data matrix composed of 50 genes from the 17 selected taxa (15). Gene sequences from five key taxa were obtained through an automated polymerase chain reaction and sequencing approach we devised for the systematic amplification of large amounts of gene sequence data from cDNA of any metazoan (15) (table S2). Gene sequences from the 12 other taxa were retrieved through bioinformatic means from public databases (15).